

Phonon-mediated superconductivity in the Sb square-net compound LaCuSb₂Kazuto Akiba^{*} and Tatsuo C. Kobayashi*Graduate School of Natural Science and Technology, Okayama University, Okayama 700-8530, Japan*

(Received 19 April 2023; accepted 24 May 2023; published 9 June 2023)

We investigated the electronic structure and superconducting properties of single-crystalline LaCuSb₂. The resistivity, magnetization, and specific heat measurements showed that LaCuSb₂ is a bulk superconductor. The observed Shubnikov–de Haas oscillation and magnetic field dependence of the Hall resistivity can be reasonably understood assuming a slightly hole-doped Fermi surface. An electron-phonon coupling calculation clarified the difference from the isostructural compound LaAgSb₂, indicating that (i) low-frequency vibration modes related to the interstitial layer sandwiched between the Sb square nets significantly contribute to the superconductivity and (ii) carriers with sizable electron-phonon coupling distribute isotropically on the Fermi surface. These are assumed to be the origin of the higher superconducting transition temperature compared with LaAgSb₂. We conclude that the superconducting properties of LaCuSb₂ can be understood within the framework of the conventional phonon-mediated mechanism.

DOI: [10.1103/PhysRevB.107.245117](https://doi.org/10.1103/PhysRevB.107.245117)**I. INTRODUCTION**

The relationship between superconductivity (SC) and other ordered states can provide new insights into the mechanism of the SC. For example, a number of so-called unconventional superconductors, whose properties cannot be understood based on the conventional phonon-mediated mechanism, have been discovered adjacent to an ordered state in the phase diagram. Heavy-fermion systems allow the exploration of unconventional SC near the quantum critical point (QCP) of a magnetic order, at which the spin fluctuation effect plays an important role in the physical properties [1]. As the SC emerges only in the vicinity of the QCP, the phase diagram represents a characteristic domelike shape [2–4]. This fact indicates that spin fluctuation plays an important role in the pairing mechanism of this material class.

Another example is a critical point of charge order. Recent studies reported the emergence of the SC or notable enhancement of the transition temperature T_c near the critical point of a charge density wave (CDW) [5–9]. Although the possible existence of a quantum fluctuation associated with the CDW has been discussed, the origin of the enhancement of SC remains unclear. To elucidate whether there is an unconventional pairing mechanism around the CDW critical point, model materials are needed to investigate systematically the relationship between the SC and the CDW.

As a candidate material, we recently focused on the intermetallic compound LaAgSb₂. LaAgSb₂ crystallizes a tetragonal structure (space group $P4/nmm$, No. 129) with a Sb square-net structure [10]. This material class has attracted attention as an extended system possessing a Dirac fermion for the band folding of a 4⁴ square net [11–13]. LaAgSb₂ shows successive CDW transitions at $T_{CDW1} \sim 210$ K and

$T_{CDW2} \sim 190$ K at ambient pressure [14,15], which can be systematically suppressed by applying hydrostatic pressure [16,17]. We investigated the transport properties of LaAgSb₂ at high pressures and established the phase diagram and the Fermi surface (FS) subjected to pressure [18,19]. Further, we discovered SC with $T_c \sim 0.3$ K coexisting with the CDWs at ambient pressure. T_c was considerably enhanced up to 1 K only around the critical pressure of CDW1 [20]. Theoretical T_c assuming the conventional phonon-mediated mechanism cannot reproduce the 1 K order T_c and its significant suppression in the normal metallic phase above 3.2 GPa, which indicates that an additional mechanism is activated at the CDW critical point to reinforce the pairing interaction. In addition, the electron-phonon coupling (EPC) calculation has indicated that the FSs derived from p_x and p_y orbitals of the Sb square net introduce a primary contribution to the SC, whereas the contributions from the rest of the FSs are considerably smaller. This indicates that the Sb square-net structure is important not only for the emergence of linear dispersion and the nesting of CDW1 but also for the primary conduction layer of the SC. Thus, LaAgSb₂ is a promising candidate for elucidating the relationship between these orders. To understand the origin of the enhancement of T_c , a careful comparison with related materials is of primary importance.

LaCuSb₂, the target of the present study, crystallizes a structure identical to that of LaAgSb₂, which is shown in Fig. 1(a). In contrast to LaAgSb₂ and another isostructural compound, LaAuSb₂ [21–24], no CDW transition is reported at ambient pressure, and only SC at $T_c \sim 0.9$ K has been reported in polycrystalline samples by Muro *et al.* [25]. On the other hand, a recent study investigated the band structure using angle-resolved photoemission spectroscopy and the magnetotransport properties of a single crystal [26]. In that study, Chamorro *et al.* experimentally reported a Dirac-like linear dispersion, a possible weak antilocalization effect due to the two-dimensionality of the electronic structure, a linear

*akb@okayama-u.ac.jp

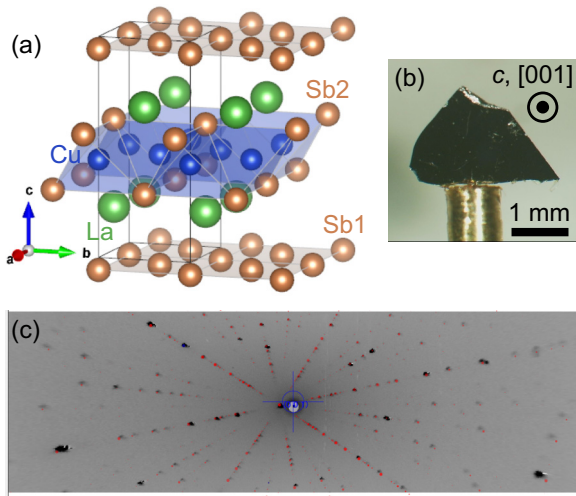


FIG. 1. (a) Crystal structure of LaCuSb_2 . (b) Photograph of a single crystal. (c) Back-reflection Laue pattern with x rays applied parallel to the $[001]$ direction. Red points represent the simulation (see the text).

magnetoresistance effect, and a Shubnikov–de Haas (SdH) oscillation with light cyclotron effective mass m_c^* . Based on the above, Chamorro *et al.* suggested a possible realization of topologically nontrivial electronic states in LaCuSb_2 . Contrary to the previous study by Muro *et al.*, however, SC has not been observed. Thus, whether the SC is intrinsic or not has not been conclusively determined.

From the viewpoint of the analogy with LaAgSb_2 and LaAuSb_2 , it is worth noting that the unit cell volume of LaCuSb_2 is 198.1 \AA^3 ($a = 4.3690 \text{ \AA}$, $c = 10.376 \text{ \AA}$) [27], which is significantly smaller than the values of 209.84 \AA^3 for LaAgSb_2 ($a = 4.3941 \text{ \AA}$, $c = 10.868 \text{ \AA}$) [18] and 205.80 \AA^3 for LaAuSb_2 ($a = 4.441 \text{ \AA}$, $c = 10.435 \text{ \AA}$) [24]. This suggests that LaCuSb_2 can be regarded as the pressurized counterpart of LaAgSb_2 and LaAuSb_2 . Thus, elucidating the physical properties of LaCuSb_2 would contribute to the understanding of the La-based intermetallic system under pressure.

In this study, we investigate the electronic structure and superconducting properties of LaCuSb_2 using experimental and computational techniques. We observe T_c at 1.0 K in electrical resistivity, magnetization, and specific heat measurements, certifying that SC is a bulk effect. In magnetotransport measurements, we reveal the field angular dependence of the SdH oscillation and positive Hall resistivity. First-principles calculation show that the experimental results are consistently understood assuming a hole-doped FS. In contrast to the case of LaAgSb_2 , EPC calculations show that (i) several low-frequency phonon modes related to the interstitial layer sandwiched between the Sb square-net layers show significant EPC and (ii) the momentum-resolved EPC distributes isotropically over the entire FS. The factors listed above double the integrated EPC strength compared with that of LaAgSb_2 , contributing to the higher T_c of LaCuSb_2 . The experimental T_c is reasonably reproduced by the McMillan-Allen-Dynes formalism; thus, we conclude that the SC of LaCuSb_2 is reasonably understood based on the conventional phonon-mediated mechanism without considering possible quantum critical phenomena.

II. EXPERIMENTAL METHOD

Single crystals of LaCuSb_2 were obtained using the Sb self-flux method. La (99.9%), Cu (99.99%), and Sb (99.9999%) with a molar ratio of 1:2:20 were placed in an alumina crucible and sealed in a quartz ampoule with argon gas. After the mixture was heated to 1150°C , it remained at that temperature for 12 h. It was then cooled to 670°C for 120 h. The flux was removed using a centrifuge separator. We obtained platelike crystals with millimeter-size dimensions, as shown in Fig. 1(b). The obtained samples were investigated by Laue diffraction measurements using IPX-YGR (IPX Co., Ltd.) based on a back-reflection configuration. Clear Laue spots were observed, as shown in Fig. 1(c), ensuring the high quality of the single crystal. The pattern was reproduced by simulations (red points) executed using QLAUE [28] assuming the reported lattice constants [27].

The resistivity measurements were performed following a standard four-terminal method. We utilized a model 370 AC resistance bridge (Lake Shore Cryotronics, Inc.) or a combined system of a 2400 sourcemeter and a 2182A nanovoltmeter (Keithley Instruments).

Magnetization measurements were performed using a direct current superconducting quantum interference device (dc-SQUID; Tristan Technologies, Inc.). A signal-pickup coil wound using a superconducting NbTi wire was connected to the sensing terminals on the dc-SQUID. The dc-SQUID was placed in a He bath, and its temperature was held at 4.2 K. The signal from the dc-SQUID was acquired with a controller via a communication cable, and we finally obtained the voltage signal, which was proportional to the change in the magnetic flux inside the pickup coil. In the magnetization measurement, we did not intentionally apply an external magnetic field. The measurements were conducted in a residual geomagnetic field.

Specific heat was measured by the relaxation method using a homemade calorimetry cell. A calibrated thermometer ($2 \text{ k}\Omega$ RuO_2 chip resistor, KOA Corporation) and a heater ($120 \text{ }\Omega$ strain gauge, Kyowa Electronic Instruments Co., Ltd.) were attached to the sample stage (a piece of Ag ribbon) with Stycast 1266. The sample stage was suspended in the vacuum space by manganin wires, which served as both thermal leak paths and current leads. The temperature dependence of the addenda heat capacity and the thermal conductivity of the manganin were determined beforehand by a measurement without sample. The sample was attached to the stage with Apiezon N grease. We measured several relaxation processes and obtained the temperature dependence of the total heat capacity, which contained both sample and addenda contributions. We finally obtained the sample heat capacity by subtracting the known addenda heat capacity.

The details of the magnetization and specific heat measurements are described in the Supplemental Material of [20].

Temperatures down to 2 K were realized by using a He-gas-flow-type optical cryostat (Oxford Instruments). Temperatures down to 50 mK were realized using a homemade dilution refrigerator. The magnetotransport properties in the presence of magnetic fields were measured using a superconducting magnet with a variable-temperature insert (Oxford Instruments, $B < 8 \text{ T}$ and $T > 1.6 \text{ K}$). The field angular

dependence of the resistivity was measured using a homemade mechanical rotator, which can uniaxially rotate the stage in the variable-temperature insert.

III. COMPUTATIONAL METHOD

The structural optimization and band structure calculation based on the density-functional theory (DFT) were performed using the QUANTUM ESPRESSO (QE) package [29,30]. We employed scalar-relativistic projector augmented-wave pseudopotentials with the Perdew-Burke-Ernzerhof exchange-correlation functional [31]. We used cutoffs of 95 and 950 Ry for the plane-wave expansions of the wave functions and charge density, respectively, and a Γ -shifted Monkhorst-Pack $10 \times 10 \times 6$ k -point grid for the self-consistent calculation. Self-consistent calculations were performed with a threshold of 1.0×10^{-8} Ry. Structural optimization was performed using convergence thresholds of 1.0×10^{-5} Ry for the total energy change and 1.0×10^{-4} Ry/bohr for the forces. Fully relaxed lattice constants and positions for La (0.25, 0.25, z_{La}) and Sb2 (0.75, 0.75, z_{Sb2}) are shown in Table I. The obtained lattice constants are close to the experimental values, $a = 4.3690$ Å, $c = 10.376$ Å [27], and the atomic coordinates agree with the previous calculation, $z_{\text{La}} = 0.2537$ and $z_{\text{Sb2}} = 0.3535$ [32]. The crystal structure was visualized by VESTA [33].

Based on the DFT calculation, we constructed the tight-binding Hamiltonian using WANNIER90 [34]. We confirmed that 16 Wannier orbitals (La d_{z^2} , La $d_{x^2-y^2}$, and Sb p) are sufficient to reproduce the DFT band structure at the Fermi level. Particularly, in the band structure calculation with orbital character projections, we employed 46 Wannier orbitals (La d , La f , Ag d , and Sb p) to represent the band character accurately. Visualization of the Wannier-interpolated FS was performed using FERMISURFER [35]. The simulations of quantum oscillation frequency F and cyclotron effective mass m_c^* were performed using the SKEAF code [36].

The simulation of electrical conductivity tensor σ was conducted based on the Boltzmann equation within the relaxation-time approximation using WANNIERTOOLS [37,38]. In the framework described above, the conductivity tensor was represented by

$$\sigma_{ij}^{(n)} = \frac{e^2}{4\pi^3} \int dk v_i^{(n)}(\mathbf{k}) \tau_n \bar{v}_j^{(n)}(\mathbf{k}) \left(-\frac{\partial f_{\text{FD}}}{\partial \epsilon} \right)_{\epsilon=\epsilon_n(\mathbf{k})}. \quad (1)$$

Herein, e , f_{FD} , and n represent the elemental charge, Fermi-Dirac distribution function, and band index, respectively. τ_n represents the relaxation time of the n th band, which is assumed to be independent of \mathbf{k} . Because of the energy derivative of the Fermi-Dirac distribution function, $\sigma_{ij}^{(n)}$ was determined by the states within the thermal energy width of $\sim k_B T$ near the Fermi level. We set $T = 10$ K to define the

TABLE I. Lattice constants a and c and atomic coordinates for La (0.25, 0.25, z_{La}) and Sb2 (0.75, 0.75, z_{Sb2}) obtained based on the structural optimization.

Space group	a (Å)	c (Å)	z_{La}	z_{Sb2}
$P4/nmm$ (No. 129)	4.423	10.293	0.2529	0.3524

thermal energy width. $\mathbf{v}^{(n)}(\mathbf{k})$ represents the velocity defined by the gradient of the energy in the reciprocal space as

$$\mathbf{v}^{(n)}(\mathbf{k}) = \frac{1}{\hbar} \frac{\partial \epsilon_n(\mathbf{k})}{\partial \mathbf{k}}. \quad (2)$$

$\bar{\mathbf{v}}^{(n)}(\mathbf{k})$ represents the weighted average of velocity over the orbit, which is defined as

$$\bar{\mathbf{v}}^{(n)}(\mathbf{k}) = \int_{-\infty}^0 \frac{dt}{\tau_n} e^{t/\tau_n} \mathbf{v}^{(n)}[\mathbf{k}(t)]. \quad (3)$$

The historical motion of $\mathbf{k}(t)$ under a magnetic field \mathbf{B} was obtained using the equation of motion

$$\frac{d\mathbf{k}(t)}{dt} = -\frac{e}{\hbar} \mathbf{v}^{(n)}[\mathbf{k}(t)] \times \mathbf{B}, \quad (4)$$

where $\mathbf{k}(t=0) = \mathbf{k}$. We adopted a 101^3 k mesh for the integration over the first Brillouin zone.

The phonon calculations were performed based on the density-functional perturbation theory (DFPT) with the optimized tetrahedron method [39] implemented in QE. A convergence threshold of 1.0×10^{-14} Ry was employed for the DFPT self-consistent iterations. The phonon dispersions were calculated using a Γ -centered 4^3 \mathbf{q} -point grid. The lattice vibrations were visualized using the phonon website [40].

EPC properties were calculated using the EPW [41] code. The electron-phonon matrix element, which describes the scattering process (from band n to m) of an electron (wave number \mathbf{k}) by a phonon (wave number \mathbf{q} and mode index ν), is defined as

$$g_{mn,\nu}(\mathbf{k}, \mathbf{q}) = \sqrt{\frac{\hbar}{2M\omega_{q\nu}}} \langle \Psi_{m\mathbf{k}+\mathbf{q}} | \partial_{q\nu} V | \Psi_{n\mathbf{k}} \rangle, \quad (5)$$

where M and \hbar are the mass of the nuclei and reduced Planck constant, respectively. $\omega_{q\nu}$ represents the frequency of a phonon with wave vector \mathbf{q} and mode ν . $|\Psi_{n\mathbf{k}}\rangle$ is the electronic wave function for band index n and wave vector \mathbf{k} with an eigenvalue of $\epsilon_{n\mathbf{k}}$. $\partial_{q\nu} V$ is the derivative of the self-consistent potential associated with a phonon with a wave vector \mathbf{q} and mode ν . Using $g_{mn,\nu}(\mathbf{k}, \mathbf{q})$, the phonon linewidth $\gamma_{q\nu}$ and EPC strength $\lambda_{q\nu}$ are represented as

$$\gamma_{q\nu} = 2\pi\omega_{q\nu} \sum_{nm} \int_{\text{BZ}} \frac{d\mathbf{k}}{\Omega_{\text{BZ}}} |g_{mn,\nu}(\mathbf{k}, \mathbf{q})|^2 \delta(\epsilon_{n\mathbf{k}} - \epsilon_F) \times \delta(\epsilon_{m\mathbf{k}+\mathbf{q}} - \epsilon_F), \quad (6)$$

$$\lambda_{q\nu} = \frac{2}{N(\epsilon_F)\omega_{q\nu}} \sum_{nm} \int_{\text{BZ}} \frac{d\mathbf{k}}{\Omega_{\text{BZ}}} |g_{mn,\nu}(\mathbf{k}, \mathbf{q})|^2 \times \delta(\epsilon_{n\mathbf{k}} - \epsilon_F) \delta(\epsilon_{m\mathbf{k}+\mathbf{q}} - \epsilon_F) = \frac{\gamma_{q\nu}}{\pi N(\epsilon_F)\omega_{q\nu}^2}, \quad (7)$$

where $N(\epsilon_F)$ is the density of states per spin at the Fermi level ϵ_F . The integral was evaluated over the Brillouin zone (BZ) with an Ω_{BZ} volume. $\delta(\epsilon)$ represents the Dirac delta function. Alternatively, we can represent the EPC strength in the \mathbf{k} space as

$$\lambda_{n\mathbf{k}} = \sum_{m\nu} \int_{\text{BZ}} \frac{d\mathbf{q}}{\Omega_{\text{BZ}}} \frac{2}{\omega_{q\nu}} |g_{mn,\nu}(\mathbf{k}, \mathbf{q})|^2 \delta(\epsilon_{m\mathbf{k}+\mathbf{q}} - \epsilon_F). \quad (8)$$

Hereafter, we omit the band index n and simply write it as $\lambda_{\mathbf{k}}$.

Using $\lambda_{q\nu}$, the Eliashberg spectral function $\alpha^2F(\omega)$ can be obtained by calculating its integrated value over the Brillouin zone as follows:

$$\alpha^2F(\omega) = \frac{1}{2} \sum_{\nu} \int_{\text{BZ}} \frac{d\mathbf{q}}{\Omega_{\text{BZ}}} \omega_{q\nu} \lambda_{q\nu} \delta(\omega - \omega_{q\nu}). \quad (9)$$

We estimated the superconducting transition temperature T_c^{MAD} using the McMillan-Allen-Dynes formula [42–44],

$$T_c^{\text{MAD}} = \frac{\omega_{\text{log}}}{1.2} \exp\left(-\frac{1.04(1+\lambda)}{\lambda - \mu_c^*(1+0.62\lambda)}\right). \quad (10)$$

Herein, λ is defined using the Eliashberg spectral function and maximum phonon frequency ω_{max} as

$$\lambda = 2 \int_0^{\omega_{\text{max}}} d\omega \frac{\alpha^2F(\omega)}{\omega}, \quad (11)$$

and ω_{log} is a logarithmic average of the phonon frequency, defined as

$$\omega_{\text{log}} = \exp\left(\frac{2}{\lambda} \int_0^{\omega_{\text{max}}} d\omega \ln \omega \frac{\alpha^2F(\omega)}{\omega}\right). \quad (12)$$

μ_c^* represents the Coulomb pseudopotential, which is treated as an empirical parameter to express the Coulomb interaction. For typical metals, μ_c^* is known to take values around 0.1 [45]. In the present study, we assumed $\mu_c^* = 0.1$.

We used coarse $8^3 \mathbf{k}$ and $4^3 \mathbf{q}$ meshes for the initial calculation of the electronic Hamiltonian, dynamical matrix, and electron-phonon matrix. To calculate the EPC properties on arbitrary, dense Brillouin zone grids, an interpolation scheme described in [46] was applied using EPW. In this procedure, we used 16 Wannier orbitals. The integrations over the Brillouin zone were performed on uniform $75^3 \mathbf{k}$ and $15^3 \mathbf{q}$ meshes. The Dirac delta functions were smeared with widths of 25 meV for electrons and 0.05 meV for phonons.

IV. RESULTS

First, we show the temperature dependence of in-plane resistivity ρ in Fig. 2(a). Metallic behavior without any indication of phase transition is exhibited, and a zero-resistivity state emerges below 1.0 K, as seen in the low-temperature data in Fig. 2(b). The onset of the resistivity drop is consistent with that of the polycrystalline sample [25]. Accompanied by the resistivity drop, the magnetization exhibits a distinct and abrupt anomaly, as shown in Fig. 2(c), which is ascribed to the Meissner effect. Additionally, the thermodynamic evidence of the SC is depicted by a sudden change in the molar specific heat c at 1.0 K, as shown in Fig. 2(d). The results described above demonstrate that LaCuSb₂ is a bulk superconductor.

From the specific heat data, we can obtain quantitative information. When the temperature T is sufficiently lower than the Debye temperature, c is represented as $c = \alpha/T^2 + \beta T^3 + \gamma T$, where the first, second, and third terms represent the nuclear, phonon, and electron contributions, respectively. From the c/T - T^2 plot shown in Fig. 2(e), we can obtain the coefficients $\beta = 338 \pm 7 \mu\text{J mol}^{-1} \text{K}^{-4}$ and $\gamma = 4.65 \pm 0.03 \text{ mJ mol}^{-1} \text{K}^{-2}$.

Additionally, we can recognize an upturn below 0.4 K, which is scaled by α/T^2 . This is ascribed to the tail of

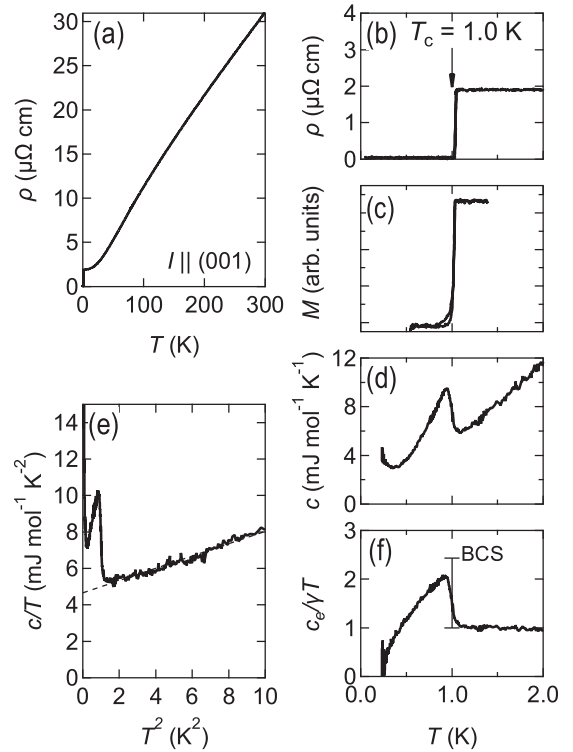


FIG. 2. (a) Temperature dependence of resistivity ρ . Superconducting transition at $T_c = 1.0$ K in (b) ρ , (c) magnetization M , and (d) specific heat c . (e) Plot of c/T as a function of T^2 . Extrapolation of the linear dependence to 0 K (dashed line) yields the electron-specific heat coefficient $\gamma = 4.65 \text{ mJ mol}^{-1} \text{K}^{-2}$. (f) Temperature dependence of $c_e/(\gamma T)$, where c_e is obtained by subtracting nuclear and lattice contributions from c (see the text). The vertical scale represents the jump expected from BCS theory.

the Schottky-type nuclear specific heat caused by an electric quadrupole splitting, which has been observed in isostructural LaAgSb₂ [20]. From curve fitting below 0.4 K, we obtained the coefficient $\alpha = 259.4 \pm 0.5 \mu\text{J mol}^{-1} \text{K}$. We have confirmed that the α value is reasonably explained by nuclear quadrupole resonance frequencies obtained with first-principles calculations.

Using the obtained coefficients α and β , we calculated the electronic specific heat c_e by subtracting the nuclear and phononic contributions from c . Figure 2(f) shows the temperature dependence of $c_e/(\gamma T)$. The observed jump in $c_e/(\gamma T)$ at 1.0 K is 1.09. Although this is slightly smaller than the value of 1.43 expected by BCS theory, the accordance is assumed to be reasonable.

In the following, we describe the magnetotransport properties. Figure 3(a) shows the in-plane magnetoresistivity ρ_{xx} and Hall resistivity ρ_{yx} at 1.6 K. Herein, B was applied along the [001] direction. ρ_{xx} shows a weak positive magnetoresistance effect, $\Delta\rho/\rho = [\rho_{xx}(B) - \rho_{xx}(0)]/\rho_{xx}(0) \sim 0.27$. In this study, we did not observe the pronounced increase in ρ_{xx} at the weak magnetic field reported previously [26], which was interpreted as a possible weak antilocalization effect. ρ_{yx} is positive up to 8 T, which indicates that the contribution of a holelike orbit is dominant. We note that a previous study reported negative ρ_{yx} under similar conditions [26], which

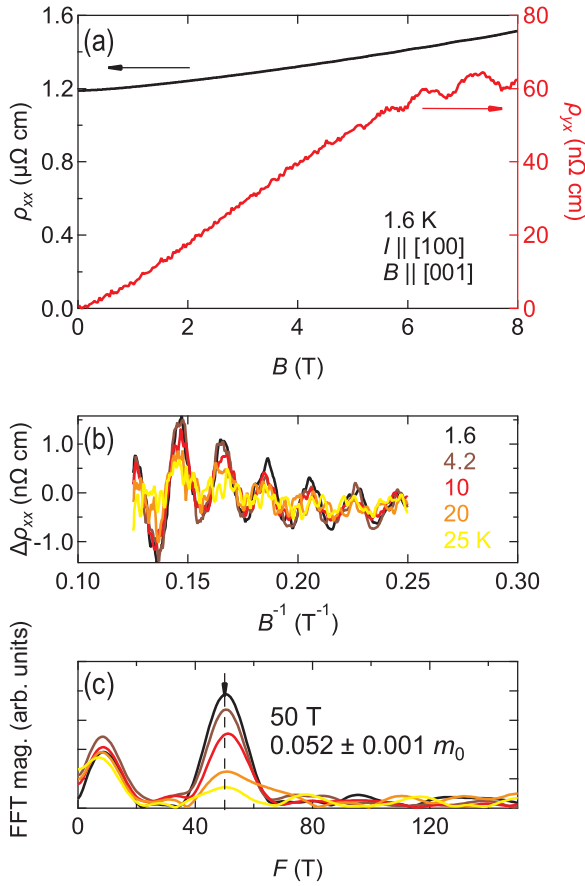


FIG. 3. (a) Magnetoresistivity ρ_{xx} (left axis) and Hall resistivity ρ_{yx} (right axis) at 1.6 K. (b) Oscillating component $\Delta\rho_{xx}$ superposed on ρ_{xx} as a function of B^{-1} at various temperatures. (c) Fast Fourier transform (FFT) magnitude of $\Delta\rho_{xx}$ at the temperatures listed in (b). The solid arrow indicates the peak at 50 T with a cyclotron effective mass of $0.052m_0$.

apparently contradicts the present results. We show subsequently that the positive ρ_{yx} is supported by the FS geometry determined in the present study. Additionally, ρ_{yx} shows non-linear behavior as a function of B , as marked in the high-field region. The possible origin of this nonlinearity will be discussed later.

We focus now on the SdH oscillations superimposed on ρ_{xx} . Figure 3(b) shows the oscillating component $\Delta\rho_{xx}$ at various temperatures. $\Delta\rho_{xx}$ was obtained by subtracting the polynomial background from ρ_{xx} . The amplitude systematically decreases as the temperature increases, which is expected from the conventional Lifshitz-Kosevich formula [47]. From the fast Fourier transform spectra shown in Fig. 3(c), we identify a single frequency of $F = 50$ T with $m_c^* = 0.052 \pm 0.001 m_0$, where m_0 represents the bare mass of the electron. The light m_c^* is consistent with that of a previous report [26].

To obtain the geometrical information about the FS, we investigated the field angular dependence of the SdH frequency. Herein, the electric current I was applied along [100], and B was rotated from [001] toward [010]. B is always perpendicular to I in this measurement. We define θ as an angle measured from [001]. Figure 4(a) shows $\Delta\rho/\rho$ for various

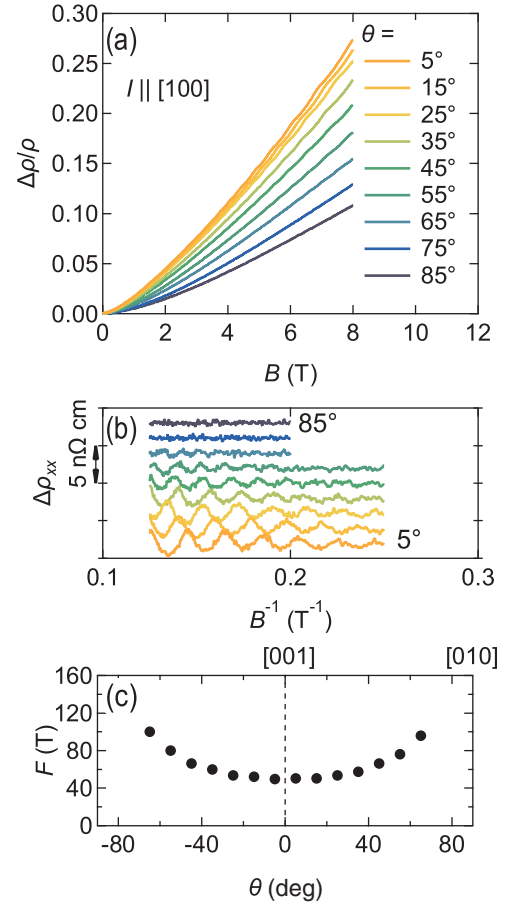


FIG. 4. (a) Magnetoresistance effect $\Delta\rho/\rho$ at various magnetic field angles. The angle θ is measured from [001]. (b) Oscillating component $\Delta\rho_{xx}$ at the θ shown in (a). The data are vertically shifted for clarity. (c) Field angular dependence of the Shubnikov-de Haas frequency F .

θ . The magnetoresistance effect is maximized (minimized) at $\theta \sim 0^\circ$ (90°). The SdH oscillation gradually becomes weak as θ increases, and we cannot discern the oscillating component at $\theta > 65^\circ$. The field angular dependence of F is summarized in Fig. 4(c), which suggests that the observed FS has cylindrical or elongated ellipsoidal shapes.

V. DISCUSSION

In the following parts, we interpret our experimental results using first-principles calculations. Figure 5(a) shows the band structure of LaCuSb₂. The horizontal dashed line ($\epsilon - \epsilon_F = 0$ eV) represents the Fermi level. Herein, we can see that the spin-orbit coupling (SOC) can hardly modify the band structure at the Fermi level. Thus, we adopted a band structure without SOC in the following discussion. The band structure has features in common with that of isostructural LaAgSb₂, which is shown in the Supplemental Material [48]. As shown in Fig. 5(b), the major contribution to the density of states D around the Fermi level comes from the p -like orbital of Sb, which corresponds to more than 50% of the total D .

We attempted to determine the geometry of the FS based on the quantum oscillation. Figure 6(a) shows the FS of

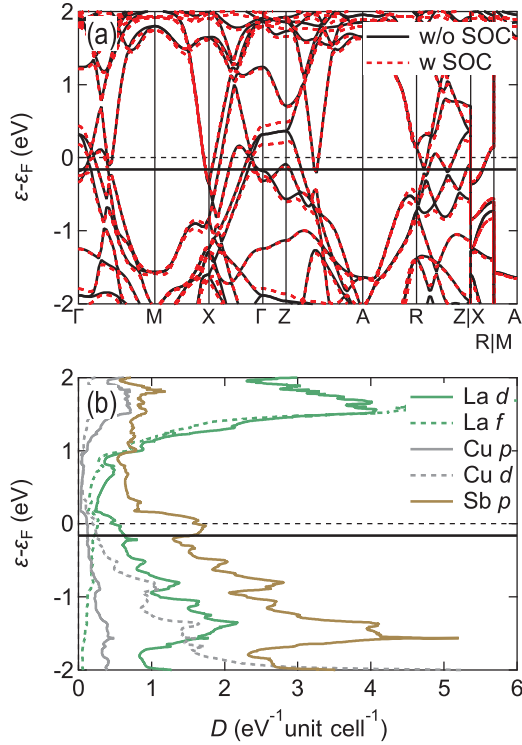


FIG. 5. (a) Electronic band structure and (b) orbital-projected density of states D . The energetic origin (horizontal dashed line) is the Fermi level ϵ_F . The horizontal solid line indicates the hole-doped case to reproduce the experimental results (see the text). The solid black and dashed red band structures in (a) indicate the cases without and with spin-orbit coupling, respectively.

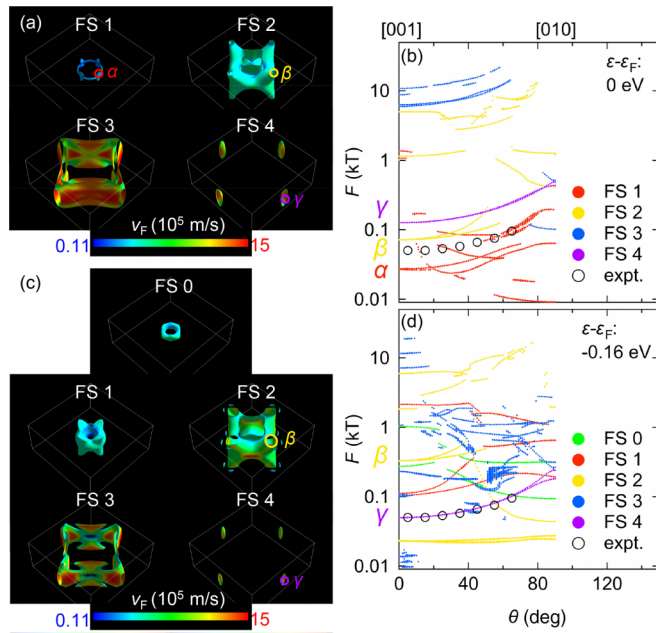


FIG. 6. (a) Fermi surface of the undoped case. (b) Calculated SdH frequencies based on the Fermi surface shown in (a). (c) Fermi surface of the hole-doped case with a Fermi level shift of -0.16 eV. (d) Calculated SdH frequencies based on the Fermi surface shown in (c). The large open symbols in (b) and (d) represent the experimental (expt.) result.

TABLE II. Representative SdH frequency F and cyclotron effective mass m_c^* at $\theta = 0^\circ$ in the case with $\epsilon - \epsilon_F = 0$ eV. The values in the square brackets indicate the case with $\epsilon - \epsilon_F = -0.16$ eV.

Label	F (kT)	m_c^* (in units of m_0)
α	0.027	0.22
β	0.072 [0.33]	0.16 [0.22]
γ	0.13 [0.050]	0.065 [0.045]

LaCuSb₂, in which the Fermi level is set at $\epsilon - \epsilon_F = 0$ eV in Fig. 5(a). In the case of the aforementioned undoped condition, there are four FSs labeled FS 1–4: the first two are holes, and the remaining two are electron surfaces. FS 1 is tiny and can thus vanish by a slight upward shift of the Fermi level. Although the overall features of FSs 2–4 are similar to those of LaAgSb₂, FS 2 shows a complex three-dimensional geometry compared with the cylindrical shape in LaAgSb₂. The obtained FS is consistent with previous studies [32,49]. Figure 6(b) shows the field angular dependence of SdH frequencies calculated based on the FS shown in Fig. 6(a). Solid (open) symbols represent the computational (experimental) results. Around $\theta \sim 0^\circ$, the calculation has no corresponding cross sections. This suggests that the actual Fermi level slightly deviates from the calculation, presumably owing to unintentional doping caused by an imperfect stoichiometry. We can assume that branches α , β , and γ are possible candidates for the experimentally observed SdH oscillation because they show θ dependences similar to those of the experimental results. The corresponding cross sections for these branches are shown in Fig. 6(a), and the expected F and m_c^* are listed in Table II. From the calculation, the m_c^* values of α and β are expected to be $0.22m_0$ and $0.16m_0$, respectively, and only γ can have $0.01m_0$ -order m_c^* . Thus, we attempted to shift the Fermi level within the rigid band approximation to reproduce the experimental SdH data using the γ branch. The results are shown in Fig. 6(d), and the corresponding FSs are shown in Fig. 6(c). This required an energy shift of $\epsilon - \epsilon_F = -0.16$ eV, which is shown by the horizontal solid line in Fig. 5. As seen in Figs. 6(c) and 6(d), the hole (electron) FS gets fatter (thinner) with hole doping, and an additional hole surface labeled FS 0 emerges. This shift of ϵ_F corresponds to a change of approximately 0.2 electron and hole per unit cell, as described in the Supplemental Material [48]. As shown in Table II, the recalculated F and m_c^* of the γ branch are 50 T and $0.045m_0$, respectively, which show reasonable agreement with the experimental value of 50 T and $0.052m_0$. From the results presented above, we can conclude that FS 4 is the most likely cause of the observed SdH oscillation.

To gain more insights into the FS, we calculated the conductivity tensors and magnetic field dependence of Hall resistivity within the relaxation time approximation. Figure 7(a) represents the electrical conductivity and Hall conductivity divided by the relaxation time ($\sigma_{xx,xy}/\tau$) in the undoped ($\epsilon - \epsilon_F = 0$ eV) and hole-doped ($\epsilon - \epsilon_F = -0.16$ eV) cases. Herein, we assume that τ is independent of the band index. Based on these data, we can calculate the theoretical Hall response [$\rho_{yx}\tau = \sigma_{xy}\tau/(\sigma_{xx}^2 + \sigma_{xy}^2)$] for each case, as shown in Fig. 7(b). The calculation supports the fact

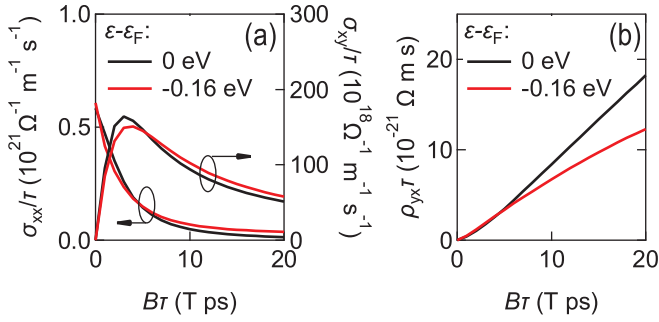


FIG. 7. (a) Calculated conductivity tensors $\sigma_{xx,xy}/\tau$ as a function of $B\tau$ in the relaxation time approximation. The curves shown in black (red) represent undoped (hole-doped) cases. (b) Calculated Hall resistivity $\rho_{yx}\tau = \sigma_{xy}\tau/(\sigma_{xx}^2 + \sigma_{xy}^2)$. The curves shown in black (red) represent undoped (hole-doped) cases.

that the Hall resistivity is positive, which is consistent with the experimental results shown in Fig. 3(a). Additionally, the nonlinearity of $\rho_{yx}\tau$ is more prominent in the hole-doped case, which qualitatively agrees with the experimental results. Thus, our experimental results can be interpreted based on the slightly hole-doped FS shown in Fig. 6(c).

Herein, we comment on the orbital character of the FS. Figures 8(a)–8(f) show the orbital projections on the band structure. FSs 3 and 4 have a Dirac-like steep dispersion (around the X and R points and along the Γ - M and Z - A paths) and consist of intensive p_x - and p_y -like characters of Sb1 with slight hybridization of La d . The emergence of this band crossing can be understood by the band folding of the 4^4 square-net structure [11–13]. Owing to the steep dispersion, the Fermi velocities v_F of these FSs are higher than the others, as indicated by the color code in Figs. 6(a) and 6(c). Conversely, FSs 0–2 consist of the orbitals of the remaining atoms (i.e., La d , Cu d , Sb2 p) and Sb1 p_z . Among them, La d and Sb2 p are particularly intensive, while Cu d and Sb1 p_z are relatively minor. Considering the above, we can reasonably assert that the electronlike surfaces mainly derive from the Sb1 square-net layer and the holelike surfaces derive from the interstitial structure between the Sb1 square nets in real space. An almost equivalent discussion applies in the case of LaAgSb₂, whose orbital-projected band structure is shown in the Supplemental Material [48].

As the position of the Fermi level has been identified above, we can estimate the bare electron specific heat coefficient γ_{bare} without any many-body effects using the calculated density of states. Using $D = 3.0 \text{ eV}^{-1} \text{ unit cell}^{-1}$ at $\epsilon - \epsilon_F = -0.16 \text{ eV}$, we obtain $\gamma_{\text{bare}} = 3.5 \text{ mJ mol}^{-1} \text{ K}^{-2}$. The difference between the experimental γ and γ_{bare} should represent the mass enhancement achieved by the many-body effect, which in the present case was mainly derived from the electron-phonon interactions. We defined the dimensionless EPC strength λ as $\gamma = \gamma_{\text{bare}}(1 + \lambda)$ and obtained $\lambda = 0.33$. The EPC should also cause an enhancement of m_c^* . Using the bare cyclotron effective mass $m_c^* = 0.045m_0$ for the γ branch and $\lambda = 0.33$, the enhanced mass should be $0.06m_0$. While the experimentally observed $m_c^* = 0.052m_0$ was slightly less than that expected, the general trend did not contradict the approximate estimation presented above.

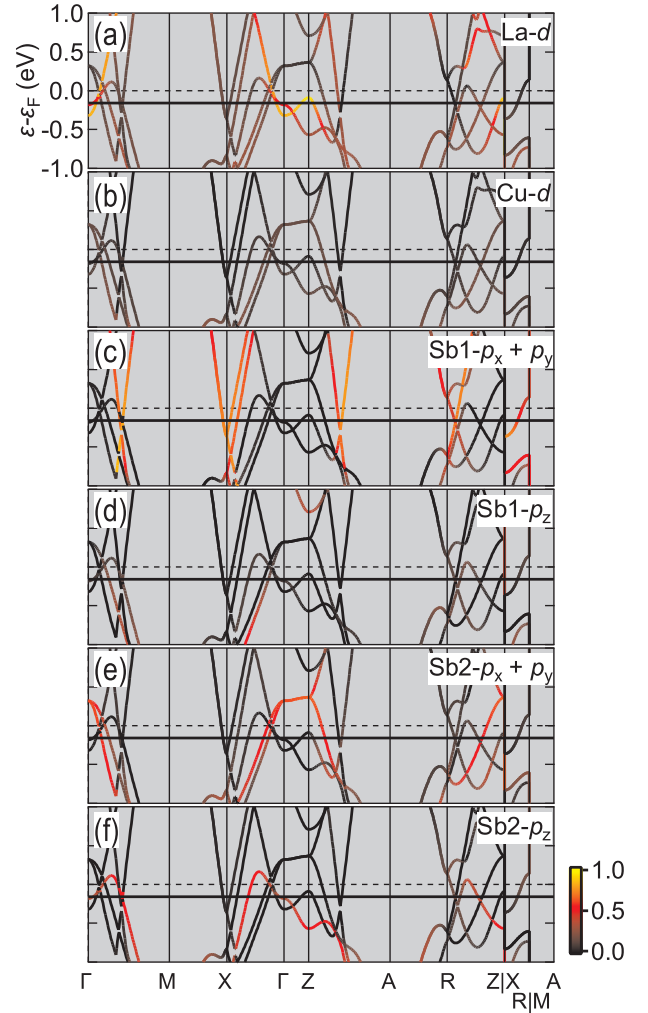


FIG. 8. Orbital-projected band structure for (a) La d , (b) Cu d , (c) Sb1 $p_x + p_y$, (d) Sb1 p_z , (e) Sb2 $p_x + p_y$, and (f) Sb2 p_z . The color code indicates the ratio of the corresponding orbital characters.

In the following, we discuss whether the observed SC can be explained by conventional phonon-mediated mechanism. Figure 9(a) shows the phonon dispersion of LaCuSb₂. The phonon bands spread up to 22 meV, and their energy scale is similar to that of LaAgSb₂. In the present case, however, we can see several phonon bands located at relatively low frequencies around 5 meV which are not observed in the phonon dispersion of LaAgSb₂. As shown in the phonon density of states in the Supplemental Material [48], lattice vibrations related to Sb2 and Cu atoms are primarily responsible for the low-frequency modes.

In the remainder, we focus on the EPC properties. Herein, we performed the calculation based on the hole-doped FS [Fig. 6(c)]. The color and radius of the symbols in Fig. 9(a) show the EPC strength $\lambda_{q\nu}$ for each q and ν . For comparison, we also show an equivalent plot for LaAgSb₂ at ambient pressure in the Supplemental Material [48]. In both cases, we can see the relatively strong EPC in optical phonons with energies in the range of 10–15 meV near the zone center. The intense EPC dominantly contributes to the Eliashberg spectral function divided by the phonon frequency $\alpha^2F(\omega)/\omega$, as shown

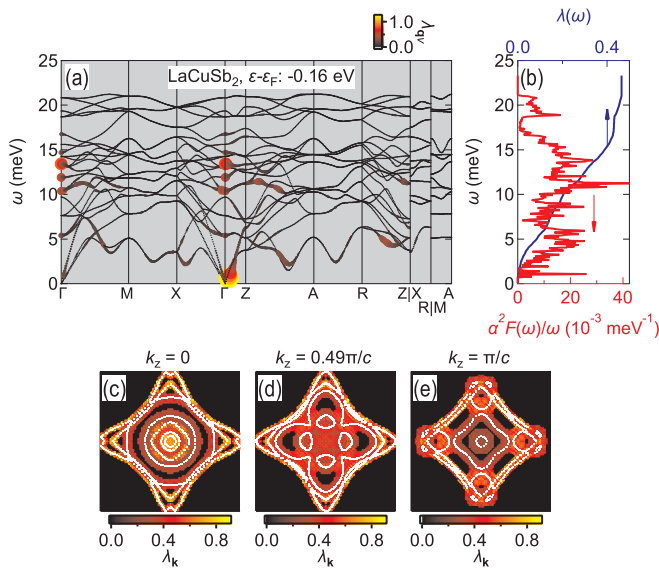


FIG. 9. (a) Phonon dispersion and electron-phonon coupling strength λ_{qv} projected on the \mathbf{q} space, where \mathbf{q} and v represent the wave vector and mode index of the corresponding phonon, respectively. The color code and symbol size indicate the magnitude of λ_{qv} . (b) Eliashberg spectral function divided by phonon frequency $\alpha^2F(\omega)/\omega$ (bottom axis) and integrated electron-phonon coupling strength $\lambda(\omega)$ (top axis). Electron-phonon coupling strength λ_k projected on the k_{xy} plane at (c) $k_z = 0$, (d) $k_z = 0.49\pi/c$, and (e) $k_z = \pi/c$. Color-coded and white symbols indicate the magnitude of λ_k and the cross section of the FS, respectively.

in Fig. 9(b), and thus results in the notable enhancement of integrated EPC strength $\lambda(\omega)$ [top axis in Fig. 9(b)] in this energy region.

The important point to note in LaCuSb₂ is that the low-frequency phonon modes mentioned above show substantial EPC, which results in a secondary peak structure in $\alpha^2F(\omega)/\omega$ at approximately 5 meV. In the Supplemental Material [48], we visualize the lattice vibrations at representative \mathbf{q} points associated with intensive EPC. It is shown that the low-frequency modes (e.g., points D-G indicated in the Supplemental Material [48]) are relevant to atomic motions within the interstitial layer, which is consistent with the atom-projected density of states.

The theoretical EPC strength was estimated to be $\lambda = 0.465$; this value is slightly higher than but shows reasonable agreement with the experimental value of $\lambda = 0.33$. The theoretical λ value is approximately doubled compared with $\lambda = 0.237$ in LaAgSb₂ at ambient pressure [20]. In the case of LaAgSb₂, the contribution to λ up to 10 meV is only 0.044 (19% of the total λ). By contrast, it reaches 0.21 (44%) in the case of LaCuSb₂. We also note that the contribution to λ above 10 meV is comparable in the LaCuSb₂ (0.26) and LaAgSb₂ (0.19) cases. The results indicate that the additional contribution from the low-frequency phonon modes is crucial for the enhancement of T_c in LaCuSb₂.

Figures 9(c)–9(e) shows the cross section of the FS (white symbols) and distribution of the EPC strength λ_k in \mathbf{k} space (color-coded symbols). Compared with the case of LaAgSb₂ shown in the Supplemental Material [48], λ_k is less sensitive to the FS (i.e., more isotropic), and the strength of λ_k is typically higher. Notably, the magnitude of λ_k of the hole surfaces (located inside the hollow-shaped FS) has values comparable to those of electron surfaces. This is in contrast to the case of LaAgSb₂ in which only electron FSs with intense $p_x + p_y$ Sb1 characters have significant EPC. The above supports the fact that not only Sb1 square-net layers but also the interstitial layers contribute to the superconducting properties in LaCuSb₂.

Finally, we deduced the theoretical T_c value based on the McMillan-Allen-Dynes formalism to be $T_c^{\text{MAD}} = 0.93$ K, using $\lambda = 0.465$, logarithmic average frequency $\omega_{\text{log}} = 103.5$ K, and typical Coulomb pseudopotential $\mu^* = 0.1$. The correspondence with the experimental value ($T_c = 1.0$ K) is quite reasonable. Thus, we conclude that the SC of LaCuSb₂ derives from the conventional phonon-mediated mechanism and seems to be less involved with the criticality of a CDW order.

VI. CONCLUSIONS

In conclusion, we investigated the electronic structure and superconducting properties of single-crystalline LaCuSb₂. We certified using resistivity, magnetization, and specific heat measurements that superconductivity is a bulk effect. We observed the Shubnikov–de Haas oscillation at the frequency of 50 T and obtained an effective cyclotron mass of $0.052m_0$, which agreed with the findings of a previous study. In contrast to the previous study, we observed monotonic field dependence of the magnetoresistivity and positive Hall resistivity. We showed that the hole-doped condition, which may be due to the imperfect stoichiometry, explained the experimental results. Based on the electronic structure determined above, we investigated the electron-phonon coupling properties to understand the superconductivity in LaCuSb₂. The results clarify the difference from LaAgSb₂ that (i) the vibration modes derived from the interstitial layer sandwiched between the Sb square nets show sizable electron-phonon coupling and (ii) the momentum-resolved electron-phonon couplings distributed over the entire Fermi surface, i.e., all carriers, contribute equally to the SC. These facts are ascribed to be the origin of the enhanced superconducting transition temperature compared with LaAgSb₂. Further, we showed that the theoretical superconducting transition temperature estimated by the McMillan-Allen-Dynes formula reasonably reproduced the experimental results. Our study concludes that the SC of LaCuSb₂ can be understood within the conventional framework of the phonon-mediated pairing mechanism.

ACKNOWLEDGMENTS

This research was supported by JSPS KAKENHI Grants No. 19K14660, No. 21H01042, and No. 22K14006.

[1] T. Moriya, *Spin Fluctuation in Itinerant Electron Magnetism* (Springer, Berlin, 1985).

[2] R. Movshovich, T. Graf, D. Mandrus, J. D. Thompson, J. L. Smith, and Z. Fisk, *Phys. Rev. B* **53**, 8241 (1996).

- [3] F. Grosche, S. Julian, N. Mathur, and G. Lonzarich, *Phys. B (Amsterdam, Neth.)* **223–224**, 50 (1996).
- [4] N. D. Mathur, F. M. Grosche, S. R. Julian, I. R. Walker, D. M. Freye, R. K. W. Haselwimmer, and G. G. Lonzarich, *Nature (London)* **394**, 39 (1998).
- [5] E. Morosan, H. W. Zandbergen, B. S. Dennis, J. W. G. Bos, Y. Onose, T. Klimczuk, A. P. Ramirez, N. P. Ong, and R. J. Cava, *Nat. Phys.* **2**, 544 (2006).
- [6] A. F. Kusmartseva, B. Sipos, H. Berger, L. Forró, and E. Tutiš, *Phys. Rev. Lett.* **103**, 236401 (2009).
- [7] T. Gruner, D. Jang, Z. Huesges, R. Cardoso-Gil, G. H. Fecher, M. M. Koza, O. Stockert, A. P. Mackenzie, M. Brando, and C. Geibel, *Nat. Phys.* **13**, 967 (2017).
- [8] K. Y. Chen, N. N. Wang, Q. W. Yin, Y. H. Gu, K. Jiang, Z. J. Tu, C. S. Gong, Y. Uwatoko, J. P. Sun, H. C. Lei, J. P. Hu, and J.-G. Cheng, *Phys. Rev. Lett.* **126**, 247001 (2021).
- [9] F. H. Yu, D. H. Ma, W. Z. Zhuo, S. Q. Liu, X. K. Wen, B. Lei, J. J. Ying, and X. H. Chen, *Nat. Commun.* **12**, 3645 (2021).
- [10] M. Brylak, M. H. Möller, and W. Jeitschko, *J. Solid State Chem.* **115**, 305 (1995).
- [11] R. Hoffmann, *Angew. Chem., Int. Ed. Engl.* **26**, 846 (1987).
- [12] S. Klemenz, S. Lei, and L. M. Schoop, *Annu. Rev. Mater. Res.* **49**, 185 (2019).
- [13] S. Klemenz, A. K. Hay, S. M. L. Teicher, A. Topp, J. Cano, and L. M. Schoop, *J. Am. Chem. Soc.* **142**, 6350 (2020).
- [14] K. D. Myers, S. L. Bud'ko, I. R. Fisher, Z. Islam, H. Kleinke, A. H. Lacerda, and P. C. Canfield, *J. Magn. Magn. Mater.* **205**, 27 (1999).
- [15] C. Song, J. Park, J. Koo, K.-B. Lee, J. Y. Rhee, S. L. Bud'ko, P. C. Canfield, B. N. Harmon, and A. I. Goldman, *Phys. Rev. B* **68**, 035113 (2003).
- [16] S. L. Bud'ko, T. A. Wiener, R. A. Ribeiro, P. C. Canfield, Y. Lee, T. Vogt, and A. H. Lacerda, *Phys. Rev. B* **73**, 184111 (2006).
- [17] M. S. Torikachvili, S. L. Bud'ko, S. A. Law, M. E. Tillman, E. D. Mun, and P. C. Canfield, *Phys. Rev. B* **76**, 235110 (2007).
- [18] K. Akiba, H. Nishimori, N. Umeshita, and T. C. Kobayashi, *Phys. Rev. B* **103**, 085134 (2021).
- [19] K. Akiba, N. Umeshita, and T. C. Kobayashi, *Phys. Rev. B* **105**, 035108 (2022).
- [20] K. Akiba, N. Umeshita, and T. C. Kobayashi, *Phys. Rev. B* **106**, L161113 (2022).
- [21] C. N. Kuo, D. Shen, B. S. Li, N. N. Quyen, W. Y. Tzeng, C. W. Luo, L. M. Wang, Y. K. Kuo, and C. S. Lue, *Phys. Rev. B* **99**, 235121 (2019).
- [22] L. Xiang, D. H. Ryan, W. E. Straszheim, P. C. Canfield, and S. L. Bud'ko, *Phys. Rev. B* **102**, 125110 (2020).
- [23] F. Du, H. Su, S. S. Luo, B. Shen, Z. Y. Nie, L. C. Yin, Y. Chen, R. Li, M. Smidman, and H. Q. Yuan, *Phys. Rev. B* **102**, 144510 (2020).
- [24] G. Lingannan, B. Joseph, P. Vajeeston, C. N. Kuo, C. S. Lue, G. Kalaiselvan, P. Rajak, and S. Arumugam, *Phys. Rev. B* **103**, 195126 (2021).
- [25] Y. Muro, N. Takeda, and M. Ishikawa, *J. Alloys Compd.* **257**, 23 (1997).
- [26] J. R. Chamorro, A. Topp, Y. Fang, M. J. Winiarski, C. R. Ast, M. Krivenkov, A. Varykhalov, B. J. Ramshaw, L. M. Schoop, and T. M. McQueen, *APL Mater.* **7**, 121108 (2019).
- [27] O. Sologub, K. Hiebl, P. Rogl, H. Noël, and O. Bodak, *J. Alloys Compd.* **210**, 153 (1994).
- [28] <https://sourceforge.net/projects/qlaue/>.
- [29] P. Giannozzi *et al.*, *J. Phys.: Condens. Matter* **21**, 395502 (2009).
- [30] P. Giannozzi *et al.*, *J. Phys.: Condens. Matter* **29**, 465901 (2017).
- [31] We used La.pbe-spf-n-kjpaw_psl.1.0.0.UPF for La, Cu.pbe-dn-kjpaw_psl.1.0.0.UPF for Cu, and Sb.pbe-n-kjpaw_psl.1.0.0.UPF for Sb in PSLIBRARY.
- [32] P. Ruzsala, M. J. Winiarski, and M. Samsel-Czekala, *Comput. Mater. Sci.* **154**, 106 (2018).
- [33] K. Momma and F. Izumi, *J. Appl. Crystallogr.* **44**, 1272 (2011).
- [34] G. Pizzi *et al.*, *J. Phys.: Condens. Matter* **32**, 165902 (2020).
- [35] M. Kawamura, *Comput. Phys. Commun.* **239**, 197 (2019).
- [36] P. Rourke and S. Julian, *Comput. Phys. Commun.* **183**, 324 (2012).
- [37] Q. Wu, S. Zhang, H.-F. Song, M. Troyer, and A. A. Soluyanov, *Comput. Phys. Commun.* **224**, 405 (2018).
- [38] S. N. Zhang, Q. S. Wu, Y. Liu, and O. V. Yazyev, *Phys. Rev. B* **99**, 035142 (2019).
- [39] M. Kawamura, Y. Gohda, and S. Tsuneyuki, *Phys. Rev. B* **89**, 094515 (2014).
- [40] <http://henriquemiranda.github.io/phononwebsite/index.html>.
- [41] S. Poncé, E. Margine, C. Verdi, and F. Giustino, *Comput. Phys. Commun.* **209**, 116 (2016).
- [42] W. L. McMillan, *Phys. Rev.* **167**, 331 (1968).
- [43] R. C. Dynes, *Solid State Commun.* **10**, 615 (1972).
- [44] P. B. Allen and R. C. Dynes, *Phys. Rev. B* **12**, 905 (1975).
- [45] P. Morel and P. W. Anderson, *Phys. Rev.* **125**, 1263 (1962).
- [46] F. Giustino, M. L. Cohen, and S. G. Louie, *Phys. Rev. B* **76**, 165108 (2007).
- [47] D. Shoenberg, *Magnetic Oscillations in Metals* (Cambridge University Press, Cambridge, 1984).
- [48] See Supplemental Material at <http://link.aps.org/supplemental/10.1103/PhysRevB.107.245117> for equivalent theoretical calculations performed on LaAgSb₂, the effect of Fermi-level shift in LaCuSb₂, and atom-projected phonon density of states of LaCuSb₂.
- [49] I. Hase and T. Yanagisawa, *Phys. Procedia* **58**, 42 (2014).